Solvation and proton transfer in polar molecule nanoclusters

Hyojoon Kim[a] and Raymond Kapral[b]
Chemical Physics Theory Group, Department of Chemistry, University of Toronto, Toronto, Ontario M5S 3H6, Canada

(Received 2 October 2006; accepted 13 November 2006; published online 21 December 2006)

Proton transfer in a phenol-amine complex dissolved in polar molecule nanoclusters is investigated. The proton transfer rates and mechanisms, as well as the solvation of the complex in the cluster, are studied using both adiabatic and nonadiabatic dynamics. The phenol-amine complex exists in ionic and covalent forms and as the size of the cluster increases the ionic form gains stability at the expense of the covalent form. Both the adiabatic and nonadiabatic transfer reaction rates increase with cluster size. Given a fixed cluster size, the stability of the covalent state increases with increasing temperature. The proton transfer rates do not change monotonously with an increase in temperature. A strong correlation between the solvent polarization reaction coordinate and the location of the phenol-amine complex in the cluster is found. The ionic form of the complex strongly prefers the interior of the cluster while the covalent form prefers to lie on the cluster surface. © *2006 American Institute of Physics*. [DOI: 10.1063/1.2404956]

I. INTRODUCTION

The rates and mechanisms of chemical reactions in systems with nanometer-scale dimensions often differ from their bulk phase counterparts. The fact that reaction dynamics can be modified is one of the reasons why nanomaterials have attracted much attention, and considerations relating to chemical reactivity often enter in the design and synthesis of these materials.[1] In this article we focus on a specific class of nanomaterials, polar molecule clusters, and one type of reaction, proton transfer.

An understanding of how proton transfer occurs is essential for the description of many chemical and biological processes.[2–4] The rates of proton transfer reactions are strongly influenced by the solvent or other environment in which the transfer takes place, especially when the environment comprises polar molecules. Since the proton is a light particle, quantum effects on the transfer rate can be significant as indicated by the magnitude of the observed kinetic isotope effects for these reactions.[5–9] Polar molecule nanoclusters are interesting environments for the study of solvent-influenced reactions because the competition between bulk and surface forces must be accounted for in the description of the reaction dynamics and computation of the reaction rate. Clusters have been extensively studied since they lie in a regime between gas and bulk liquid or solid phases and possess unusual properties.[10–16] There have been many experimental and theoretical studies of proton transfer[17–26] and electron solvation[27,28] in clusters or reverse micelles. These systems provide interesting nanoenvironments for reactions.

In order to investigate how proton transfer dynamics is influenced by the cluster environment, we consider a model for proton transfer in a phenol-amine complex[29] dissolved in a methyl chloride polar molecule cluster. This model has been studied in both bulk solvents[29–36] and reverse micelles.[25,26] We present results for the free energy of the cluster proton transfer process, as well as estimates of the reaction rates using adiabatic dynamics and nonadiabatic quantum-classical Liouville dynamics.[37–46]

The paper is organized as follows. In Sec. II, we describe the model along with the theoretical and simulation methods used to obtain the results. Section III reports the results of our simulations and comments on the observed phenomena. Further discussion of the results and comparisons with other studies are given in Sec. IV.

II. THEORY AND METHODS

We investigate the Azzouz-Borgis model[29] for proton transfer in a hydrogen-bonded phenol-trimethylamine complex,

$$\mathrm{PhO-H\cdots NR_3} \rightleftharpoons \mathrm{PhO^- \cdots H-NR_3^+}, \tag{1}$$

but in a cluster instead of the condensed phase. This model utilizes simple empirical potential energy functions that capture the main features of the proton transfer process within the complex. The phenol and trimethylamine groups are modeled by two Lennard-Jones centers, and hydrogen bonding within the complex is described by exponential functions that account for the variation of the charge distribution which results from the motion of the proton along the axis between the phenol and amine groups. The covalent state of the complex [left side of Eq. (1)] has a molecular dipole moment of $\mu=2.5$ D, while the ionic state [right side of Eq. (1)] has $\mu=10.5$ D. To simplify the notation we denote the covalent complex state by A and the ionic complex state B, so that the reaction is $A \rightleftharpoons B$. The vibration of the internuclear separation between the phenol and amine groups in the complex is accounted for in the model and the equilibrium distance between $\mathrm{PhO\cdots NR_3}$ is 2.7 Å. We study the proton transfer process in a polar CH_3Cl cluster and vary the number of

[a]Electronic mail: hkim@chem.utoronto.ca
[b]Electronic mail: rkapral@chem.utoronto.ca

cluster solvent molecules N_s to investigate cluster size effects on the transfer rate and free energy. The CH_3Cl solvent molecules are represented by a two-site model with the bond length constrained at 1.781 Å. The interactions among solvent molecules, as well as those between the phenol-amine complex and the solvent molecules, arise from Lennard-Jones and Coulomb forces. The proton interacts with the solvent molecules via Coulomb forces.[29,30] Full details of the interaction potentials and parameters used in this study can be found in the literature.[29,30]

The Hamiltonian $\hat{H}$ of the system can be written as

$$\hat{H}(\hat{q},R) = K_S + K_C + \hat{H}_P(\hat{q},R), \tag{2}$$

where K_S and K_C are kinetic energy contributions from the solvent and heavy molecules in the complex, respectively, and the protonic Hamiltonian $\hat{H}_P$ includes the kinetic energy of proton and all interaction potentials. The set of coordinates of the solvent and complex heavy molecules is denoted by R, and the distance between the center of mass of the complex and the proton can be described by a one-dimensional position operator $\hat{q}$ since the complex is assumed to be linear with respect to the proton transfer coordinate.

It is convenient to use an adiabatic basis to solve the quantum evolution for the proton transfer. The adiabatic eigenstates $|\alpha;R\rangle$ and eigenvalues $E_\alpha(R)$ are determined from the solution of the Schrodinger equation,

$$\hat{H}_P(\hat{q},R)|\alpha;R\rangle = E_a(R)|\alpha;R\rangle, \tag{3}$$

for a fixed configuration R of the heavy molecules. In our simulations we solved this equation numerically using 12 quantum harmonic oscillator basis functions.[30,36] The Hamiltonian operator $\hat{H}$ in this adiabatic basis is diagonal and its matrix elements are given by $\langle\alpha;R|\hat{H}|\alpha;R\rangle \equiv H_\alpha(X) = P^2/2M + E_\alpha(R)$, where P denotes the set of momenta of the heavy particles and $X=(R,P)$ is a phase point. We use the simplified notation $P^2/2M$ for the kinetic energy terms $K_S + K_C = P^T M^{-1} P/2$, where M is the diagonal matrix of masses of the heavy particles and P and P^T are column and row vectors, respectively.

A. Reaction coordinate and free energy

Given a general configuration-dependent reaction coordinate denoted by $\xi(R)$, if the system is confined to adiabatic state α, the free energy along this reaction coordinate is defined by[36]

$$\beta W_\alpha(\xi') = -\ln \frac{\langle \delta(\xi(R)-\xi')\rangle_\alpha}{P_u} - \ln\langle e^{-\beta(E_\alpha - E_1)}\rangle_1, \tag{4}$$

where P_u is the uniform probability density, $\langle\cdots\rangle_\alpha = \int dX \cdots e^{-\beta H_\alpha}/\int dX e^{-\beta H_\alpha}$, and β is the inverse of Boltzmann's constant times the temperature T. The argument of the last term represents the ratio of the probability that the system is in state α to that in the ground state. We can calculate the free energy by binning the results from long *adiabatic* trajectories since the last term of Eq. (4), which is an additive constant for each α state, can be evaluated from adiabatic ground state trajectories.

We suppose that reactants and products are separated by a dividing surface at $\xi^\ddagger$ so that operators $N_A = \theta(\xi^\ddagger - \xi(R))$ and $\hat{N}_B = \theta(\xi(R) - \xi^\ddagger)$ characterize the reactant (A) and product (B) species. Given these species definitions, the equilibrium constant $K_{\rm eq}$ can be obtained from the free energy using

$$K_{\rm eq} = \frac{n_B^{\rm eq}}{n_A^{\rm eq}} = \int_{\xi^\ddagger}^{\infty} d\xi e^{-\beta W_1(\xi)} \Big/ \int_{-\infty}^{\xi^\ddagger} d\xi e^{-\beta W_1(\xi)}. \tag{5}$$

For condensed phase and cluster proton transfer processes, a convenient choice for the reaction coordinate is the solvent polarization,[47] which is defined as the difference between the solvent electrical potentials at two points in the complex.[48] This reaction coordinate monitors the effects of the solvent dynamics on the proton transfer reaction. For our system, the solvent polarization is given explicitly by[36,49]

$$\Delta E(R) = \sum_{i,a} z_a e \left(\frac{1}{|\mathbf{R}_i^a - s|} - \frac{1}{|\mathbf{R}_i^a - s'|} \right). \tag{6}$$

The sums run over all solvent molecules i and atoms a. In Eq. (6) $z_a e$ is the charge on atom a, and s and s' are two points within the complex at the center of mass and displaced by −0.56 from the center of mass, respectively, corresponding to the minima of the bare potential. We utilize this reaction coordinate and take $\xi(R) = \Delta E(R)$ in our simulations.

B. Reactive dynamics

The general expression for the time-dependent rate coefficient of the reaction in Eq. (1) used in this study was derived from the quantum reactive-flux correlation function[50] and is given by[51,52]

$$k_{AB}(t) = \frac{1}{n_A^{\rm eq}} \sum_\alpha \sum_{\alpha' \geq \alpha} (2 - \delta_{\alpha'\alpha}),$$

$$\times \int dX \, {\rm Re}\left[N_B^{\alpha\alpha'}(X,t) W_A^{\alpha'\alpha}\left(X, \frac{i\hbar\beta}{2}\right)\right]. \tag{7}$$

The spectral density function $W_A^{\alpha'\alpha}$ accounts for the quantum canonical equilibrium structure of the system at the temperature T and is used to sample initial conditions for the calculation.[52–55] In the present application to high-temperature, liquid-state clusters, the equilibrium structure of the bath degrees of freedom may be treated classically to a good approximation. Since the reaction coordinate depends on bath degrees of freedom as well, we have[9,56]

$$W_A^{\alpha'\alpha}\left(X, \frac{i\hbar\beta}{2}\right) = \dot{\xi}(R)\,\delta(\xi(R) - \xi^\ddagger)\frac{e^{-\beta H_\alpha(X)}}{Z_Q}\delta_{\alpha'\alpha}. \tag{8}$$

Here $Z_Q = \Sigma_\alpha \int dX e^{-\beta H_\alpha(X)}$ and $n_A^{\rm eq} Z_Q$ are the total and reactant partition functions, respectively. Using Eq. (8), the rate coefficient takes the form

$$k_{AB}(t) = \frac{1}{n_A^{\mathrm{eq}}} \sum_{\alpha} \int dX \, \mathrm{Re}[N_B^{\alpha\alpha}(X,t)] \times \dot{\xi}(R)\,\delta(\xi(R)-\xi^{\ddagger}) \frac{e^{-\beta H_\alpha(X)}}{Z_Q} \equiv \frac{1}{n_A^{\mathrm{eq}}} \sum_{\alpha} \langle \mathrm{Re}[N_B^{\alpha\alpha}(X,t)] \dot{\xi}(R)\,\delta(\xi(R)-\xi^{\ddagger}) \rangle. \quad (9)$$

The forward rate constant k_{AB} can be obtained from the plateau value of $k_{AB}(t)$.[57]

The evolution of the species variable $N_B^{\alpha'\alpha}(X,t)$ was computed using quantum-classical Liouville dynamics, which treats proton quantum mechanically and its environment classically, in the adiabatic basis,[43]

$$\frac{d}{dt} N_B^{\alpha'\alpha}(X,t) = \sum_{\beta\beta'} i\mathcal{L}_{\alpha'\alpha,\beta'\beta}(X) N_B^{\beta'\beta}(X,t). \quad (10)$$

The quantum-classical Liouville operator $i\mathcal{L}$ in this basis is given by $i\mathcal{L}_{\alpha\alpha',\beta\beta'}(X) = [i\omega_{\alpha\alpha'}(R) + iL_{\alpha\alpha'}(X)]\delta_{\alpha\beta}\delta_{\alpha'\beta'} - J_{\alpha\alpha',\beta\beta'}(X)$, where the evolution operator $iL_{\alpha\alpha'}$ is given by

$$iL_{\alpha\alpha'} = \frac{P}{M}\frac{\partial}{\partial R} + \frac{1}{2}[F^{\alpha}(R) + F^{\alpha'}(R)]\frac{\partial}{\partial P}. \quad (11)$$

Here the frequency $\omega_{\alpha\alpha'}(R) \equiv [E_\alpha(R) - E_{\alpha'}(R)]/\hbar$ and the Hellmann-Feynman force is $F^{\alpha} = -\langle \alpha;R|\nabla_R \hat{H}_p(\hat{q},R)|\alpha;R\rangle$. The operator J is responsible for the momentum transfer to and from the bath that accompanies nonadiabatic transitions. In the momentum-jump approximation it has the form[36,43,58]

$$J_{\alpha\alpha',\beta\beta'} \approx -\frac{P}{M}\cdot d_{\alpha\beta} e^{(1/2)S_{\alpha\beta}\cdot(\partial/\partial P)}\delta_{\alpha'\beta'} - \frac{P}{M}\cdot d^{*}_{\alpha'\beta'} e^{(1/2)S^{*}_{\alpha'\beta'}\cdot(\partial/\partial P)}\delta_{\alpha\beta}, \quad (12)$$

where $S_{\alpha\beta} = (E_\alpha - E_\beta) d_{\alpha\beta} ((P/M)\cdot d_{\alpha\beta})^{-1}$ and the nonadiabatic coupling matrix element $d_{\alpha\beta} = \langle \alpha;R|\partial/\partial R|\beta;R\rangle$.

In the adiabatic limit, there are no quantum transitions and the J term is zero. In this limit Eq. (11) reduces to the classical evolution operator on adiabatic surfaces and the evolution equation for the diagonal element of the species variable becomes

$$\frac{d}{dt} N_{B,\mathrm{aa}}^{\alpha\alpha}(X,t) = iL_{\alpha\alpha}(X) N_{B,\mathrm{aa}}^{\alpha\alpha}(X,t). \quad (13)$$

Comparisons between nonadiabatic and adiabatic dynamics will be presented in the next section.

C. Simulation details

The clusters we investigate are metastable objects that will experience evaporation of solvent molecules. However, within the temperature range studied in this paper, the lifetime of a cluster with a fixed number of solvent molecules is very long compared to the time scale of proton transfer events. The approximate cluster lifetime was found to be $\sim 10\ \mu\mathrm{s}^{-1}$ by counting the number of evaporation events in a given time interval, while the proton transfer rate, i.e., the mean time to pass between the covalent and ionic forms of the complex, was determined to be $\sim 10\ \mathrm{ns}^{-1}$. In view of this time scale separation it is possible to describe these metastable states using equilibrium statistical mechanical averages.

Liquid-state clusters were obtained by melting a face-centered cubic lattice structure of the complex and N_s solvent molecules with velocity rescaling to obtain a desired temperature T. Once a cluster with a typical liquid structure was formed, the system was further equilibrated for 50 ps using microcanonical dynamics. The equations of motion were integrated using the velocity Verlet algorithm. We have converged results with a time step of $\Delta t = 5$ fs. Bond constraints for the solvent molecules were enforced using RATTLE and SHAKE algorithms.[59,60] No potential cutoffs or boundary conditions were imposed on the cluster molecule potentials. Using this procedure an ensemble of clusters whose temperature, determined from the average kinetic energy, was within ±1 K of the desired temperature was constructed. The free energy along the polarization reaction coordinate was determined from such an ensemble of long-time adiabatic trajectories where no evaporation occurs.

Since the free energy barrier for proton transfer is high ($4k_BT - 7k_BT$) for many of the clusters studied here, we computed the proton transfer rate coefficient from the reactive-flux correlation function using blue moon sampling[61–63] which uses holonomic constraints to confine the system to the hypersurface $\Delta E = \Delta E^{\ddagger}$. The rate coefficient results were obtained from averages over approximately 1×10^5 trajectories which were propagated with a time step of $\Delta t = 10$ fs. The initial states of the ensemble members with given N_s and T were determined from approximately 1×10^4 initial configurations generated as described above but with the constraint $\Delta E = \Delta E^{\ddagger}$ imposed. For each configuration, we used ten different initial sets of velocities chosen randomly from a Gaussian distribution corresponding to the temperature T.

The evaluation of the quantum-classical Liouville evolution for the species variable was carried out using the sequential short-time propagation algorithm[64] which involves propagating an ensemble of surface-hopping trajectories. The phase space coordinates were propagated adiabatically for a molecular dynamics time step, and a phase factor was computed if the evolution was on the mean of two adiabatic surfaces. Transitions between surfaces were carried out stochastically using transition probabilities that depend on the nonadiabatic coupling matrix elements.[64] A limit was set on the maximum number of allowed nonadiabatic transitions per trajectory. No significant dependence on this limit was found if up to $n_{\max} = 6$ nonadiabatic transitions were allowed. A bound of ±5 on the weight factor was also implemented to improve the statistics.[36] Since the vast majority of nonadiabatic transitions occur around $\Delta E^{\ddagger}$, we allowed nonadiabatic transitions only within the window $\Delta E^{\ddagger} \pm 0.002$ e C/Å. The rate constant was obtained from the plateau value of the time-dependent rate coefficient using absorbing boundaries at the minima of two wells in the ground state.

III. RESULTS

The methods discussed above allow one to study both the equilibrium structure reflected in the free energy along

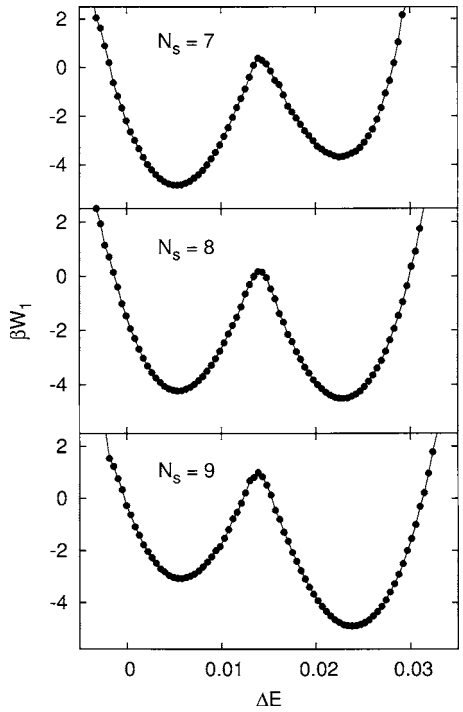

FIG. 1. Ground state free energy profiles (βW_1) as a function of the reaction coordinate ΔE for three different-sized clusters N_s=7, 8, and 9, at T=150 K.

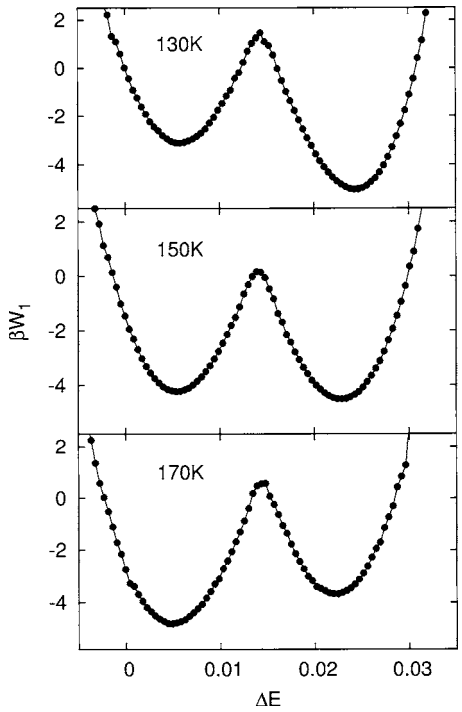

FIG. 2. Ground state free energy profiles (βW_1) as a function of the reaction coordinate ΔE for cluster size N_s=8 at three different temperatures T=130, 150, and 170 K.

the polarization reaction coordinate and the dynamical properties that determine the mechanism and rate of the cluster proton transfer process.

A. Free energy

The free energy along the reaction coordinate with the system restricted to the ground state adiabatic surface was determined using Eq. (4) by binning the results from an ensemble of long-time trajectories. The free energy curves are plotted in Fig. 1 for N_s=7, 8, and 9 solvent molecules and a temperature of T=150 K. Several features are apparent from an examination of these plots. As the number of solvent molecules increases, the ionic state gains stability. For clusters with $N_s \geqslant 8$ the ionic state is more stable than the covalent state. This trend has its origin in the enhanced ability of the larger polar molecule clusters to effectively solvate the ionic form of the phenol-amine complex. For the temperature T =150 K, the solvation structure changes its character at N_s =8, since the covalent state has a lower free energy for N_s <8.

Similar trends are seen in Fig. 2 where the cluster solvent number is fixed at N_s=8 but the temperature varies. As the temperature increases the covalent state gains stability at the expense of the ionic state. At the lower temperatures the reaction that takes the system from the covalent state to the ionic state is more exothermic. Consequently, as the temperature increases one would expect the equilibrium to shift towards reactants, as is observed. From a molecular perspective this trend has its origin in the disruption of the solvation structure of the ionic state at the higher temperatures.

From Figs. 1 and 2 we see that while the location of the well minimum of the covalent state in free energy profiles ΔE_A^m varies relatively weakly with changes in N_s and T, the position of the ionic state minimum, ΔE_B^m increases as the ionic state well depth increases. This trend is shown in Fig. 3 where ΔE_A^m and ΔE_B^m are plotted versus N_s and T. The location of the barrier top $\Delta E^{\ddagger}$ changes very little with changes in N_s and T. Consequently, $\Delta E^{\ddagger}$ may be taken to be independent of the cluster size and the temperature and, in fact, is approximately the same as that for the bulk solvent, $\Delta E^{\ddagger}$ =0.0141 e C/Å.[36]

In Fig. 4, we plot the equilibrium constant K_{eq}, which was computed using Eq. (5), as functions of N_s and $1/T$ on a semilog scale. The left panel in this figure shows that the stability of the ionic state increases with cluster size. The linear dependence of $\ln K_{eq}$ with N_s at T=150 K means that the addition of one solvent molecule increases K_{eq} by a factor of approximately 4.5 and stabilizes the ionic state by approximately 2 kJ/mol ($\sim 1.50 \times 150$ K in units of the gas constant), which can be regarded as the solvation free energy

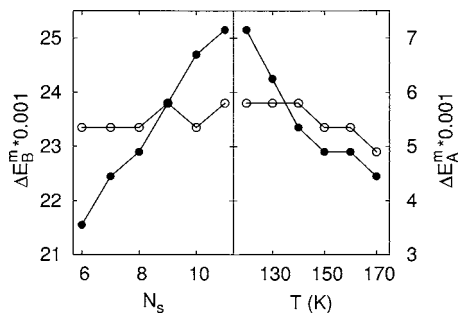

FIG. 3. Plots of the ionic state well minimum ΔE_B^m (solid circles) and the covalent state well minimum ΔE_A^m (open circles) as a function of N_s at T=150 K (left) and for N_s=8 as a function of T (right).

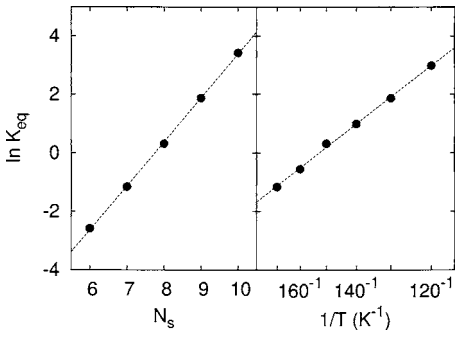

FIG. 4. Plot of the equilibrium constant K_{eq} as functions of a cluster size N_s at $T=150$ K (left) and inverse temperature $1/T$ for $N_s=8$ (right) on a semi-log scale. Dotted lines represent linear fits to the data with an equation of the form $\ln K_{eq}=a_0+a_1x$. The values of a_0 and a_1 are −11.67 and 1.50 for $x=N_s$, respectively, and −11.00 and 1677 K for $x=1/T$, respectively.

per solvent molecule. The right panel in Fig. 4 shows that $\ln K_{eq}$ is linearly dependent on the inverse temperature. From the van't Hoff equation $d\ln K_{eq}/d(1/T)=-\Delta H^{(0)}$, so the standard enthalpy difference $\Delta H^{(0)}$ between the covalent and ionic state is independent of temperature in this temperature range. We find $\Delta H^{(0)}$ is −1680 K ~ −14 kJ/mol, corresponding to an exothermic transfer reaction from the covalent to ionic state.

B. Adiabatic dynamics

Before using the quantum-classical Liouville equation to evolve the species variable $N_B=\theta(\Delta E(R)-\Delta E^{\ddagger})$, we consider adiabatic dynamics with the system confined to the ground and first excited state surfaces. Figure 5 gives plots of the free energy curves for the ground and the first excited states of the proton for $N_s=8$ and $T=150$ K. The excited state surface has a single-well form with its minimum located at the barrier top position of the ground state free energy curve. (This figure also shows the mean of these two free energy curves, which enters in the description of the nonadiabatic dynamics as discussed in the next subsection.)

Figure 6 shows the contributions to the forward time-dependent adiabatic rate coefficient $k_{AB}^{ad}(t)$ coming from the ground and excited surfaces for $N_s=8$ and $T=150$ K. The excited state contribution decays very rapidly to zero. This is expected in view of the single-well character of the excited state free energy surface which leads to rapid recrossing of the dividing surface. In contrast, the ground state curve decays more slowly to a plateau value after an initial rapid fall from its $k_{AB}^{TST}=k_{AB}(0^+)$ value. Thus, the long-time plateau value, which is determined by the ground state contribution, yields the adiabatic reaction constant k_{AB}^{ad}.

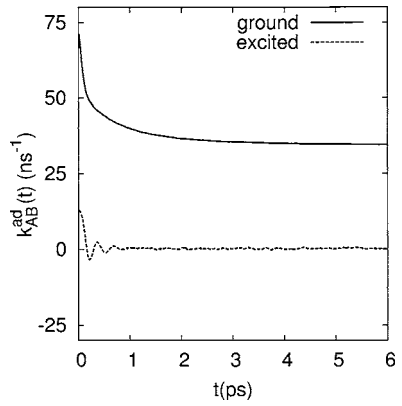

FIG. 6. Ground and excited state contributions to the forward time-dependent rate coefficient $k_{AB}^{ad}(t)$ vs time for $N_s=8$ and $T=150$ K.

The forward (k_{AB}^{ad}) and backward (k_{BA}^{ad}) adiabatic rate constants for various values of N_s (left panel) and temperature (right panel) are plotted in Fig. 7. The backward rate constant was calculated using the detailed balance condition $K_{eq}=k_{AB}^{ad}/k_{BA}^{ad}$. The forward rate constant increases and the backward rate constant decreases with increasing number of solvent molecules since large numbers of solvent molecules stabilize the ionic product state more effectively than small numbers. It is interesting to observe that the forward rate constant does not increase monotonously with temperature like the backward rate constant. This arises from the competition of two effects: a broader distribution of velocities at higher temperatures that helps the system cross the free energy barrier and the increasing height of the free energy barrier for the forward proton transfer process with increasing temperature. The total rate constant ($k_{AB}+k_{BA}$) has a maximum value for $N_s=8$ and $T=150$ K where the ionic and covalent states have nearly equal free energies. The cluster rate constants have magnitudes similar to those previously reported for clusters and bulk liquid[26,36] despite considerable differences in the system environments.

Recrossing of the dividing surface before stabilization of the system in the reactant or product states reduces the rate constant. This reduction is reflected in the transmission coefficient for adiabatic dynamics κ^{ad}, which is defined by

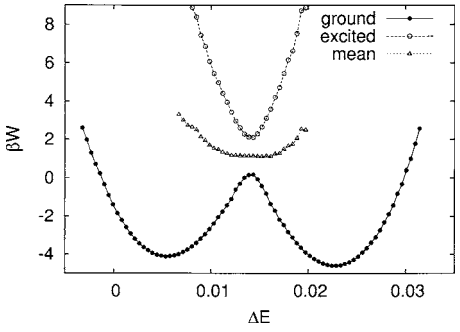

FIG. 5. Ground (solid circles) and excited (open circles) free energy (βW) profiles as a function of the reaction coordinate ΔE for clusters with $N_s=8$ and $T=150$. The mean of these two states is also plotted as open triangles.

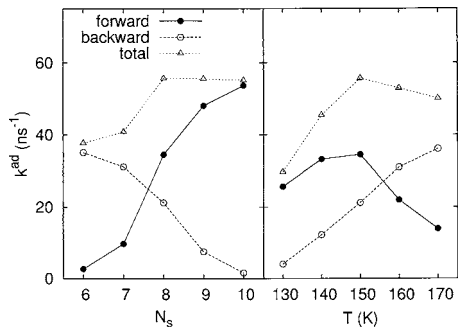

FIG. 7. Plots of the forward (k_{AB}^{ad}), backward (k_{BA}^{ad}), and total ($k_{AB}^{ad}+k_{BA}^{ad}$) adiabatic rate constants vs N_s for $T=150$ K (left) and vs T for $N_s=8$ (right).

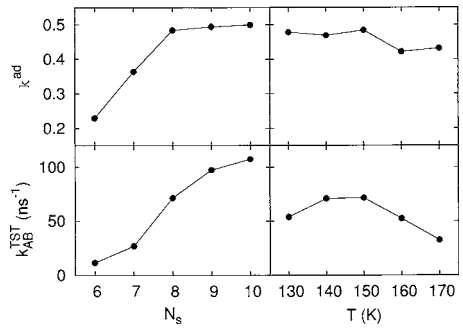

FIG. 8. Plots of the adiabatic transmission coefficient κ^{ad} (upper panels) and TST rate coefficient k_{AB}^{TST} (lower panels) as a function of N_s for $T=150$ K (left) and for $N_s=8$ as a function of T (right).

$k_{AB}^{ad}=k_{AB}^{TST}\kappa^{ad}$ and is plotted in Fig. 8 (upper panel) as functions of N_s and T. The lower panel of this figure shows the transition state theory (TST) rate constant k_{AB}^{TST}. Both κ^{ad} and k_{AB}^{TST} show similar variations with N_s but their variations with temperature are different. While κ^{ad} depends weakly on T, k_{AB}^{TST} varies more strongly and accounts for the major temperature variations of the full rate constant k_{AB}^{ad}.

One of the main differences between proton transfer in the phenol-amine complex in a nanocluster and in bulk condensed phases or in confined geometries such as micelles is the fact that nanoclusters can deform or undergo other structural changes in response to chemical transformations.[14,65] Such changes play a role in the proton transfer dynamics studied here since strong cluster shape fluctuations were observed. In addition, as in related studies,[25,26,65] our simulations have shown that the passage between the covalent and ionic states of the complex is strongly correlated with the location of the complex in the cluster. This correlation is seen in Fig. 9, which shows contour plots of the joint probability density $P(\Delta E,d)$ of ΔE and d, where d denotes the distance between the center of mass of all cluster solvent molecules and that of the phenol-amine complex.

The strong correlation between these two quantities indicates that the ionic state of the complex state prefers configurations near the center of the cluster while the covalent state of the complex prefers to reside on the cluster surface. Sample configurations of the solvation structure of the covalent and ionic states are shown in Fig. 10. In the right panel showing the solvation of the ionic state one can see that the

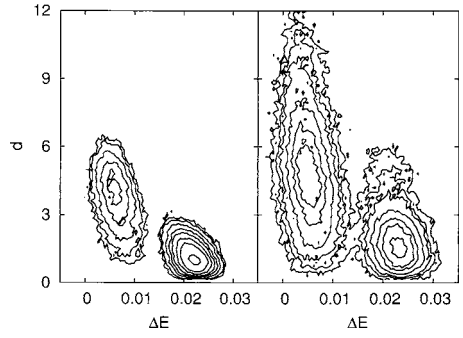

FIG. 9. Contour plots of the joint probability density $P(\Delta E,d)$ vs solvent polarization ΔE and the distance d (Å) between the center of mass of all solvent molecules and that of the complex for $N_s=7$ and $T=100$ K (left) and $N_s=11$ and $T=180$ K (right).

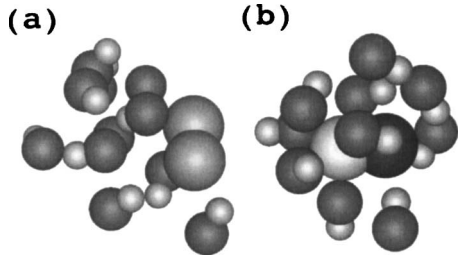

FIG. 10. Two cluster configurations for $N_s=11$ and $T=180$ K. The magnitudes of the charges on the two sites in the complex are represented by gray levels. The positively charged groups are indicated by light gray and the negatively charges groups are in dark gray. In the left (a) configuration, the complex molecule shown in gray is in the covalent state, and in the right (b) configuration, the complex shown in black and white is in the ionic state.

solvent molecules are oriented to produce strong attractive electrostatic interactions leading to the stabilization of this configuration. As the cluster size increases, the covalent state of the complex can move more freely but the ionic state is restricted to regions near the center of the cluster. This effect can be seen by comparing the results for $N_s=7$ and 11 in Fig. 9. It is also apparent that ΔE is a better reaction coordinate than d since it provides a more unambiguous distinction between reactants and products.

The contour plot in the right panel of Fig. 9 shows that the lowest free energy path from reactants (covalent state, small ΔE) to products (ionic state, large ΔE) involves the movement of the complex to the center of the cluster before the reorganization of the solvent molecules to induce a change in the polarization. Of course, for the reversible passage from products to reactants the reverse process occurs. This observation differs from that for reverse micelles,[26] where in the dominant mechanism the movement of the complex follows the solvent rearrangement.

C. Nonadiabatic dynamics

We also computed the rate constants using quantum-classical Liouville dynamics which accounts for transitions between adiabatic states.[10] In nonadiabatic dynamics, quantum transitions lead to off-diagonal species matrix elements and when the system is in such coherently coupled states the classical degrees of freedom evolve on the mean of the ground and excited adiabatic surfaces. The mean free energy curve, shown in Fig. 5 has a single minimum in contrast to that for a bulk solvent where it has a shallow double-well form.[36] This feature influences the nature and magnitude of nonadiabatic effects in this system.

The adiabatic and nonadiabatic forward rate constants are compared in Fig. 11 for various values of N_s and T. Nonadiabatic effects are small. The magnitude of nonadiabatic effects is controlled by the nonadiabatic coupling matrix elements which depend on the energy gap and coupling strength. These matrix elements are largest in the vicinity of the barrier top where the energy gap is at its smallest value. Both the excited state and mean free energy curves have single-well forms whose minima lie at the barrier top of the ground state. Consequently, one expects the nonadiabatic transitions to be largely localized in this region.

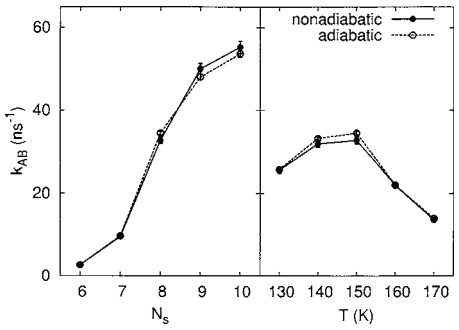

FIG. 11. Forward nonadiabatic rate constants k_{AB} for various values of N_s at $T=150$ K (left) and for $N_s=8$ at various temperatures (right). The error bars represent ±1 standard deviations. Adiabatic forward rate constants are also plotted for comparison.

The nonadiabatic coupling matrix elements are much smaller for the cluster than for the bulk phase solvent where nonadiabatic effects were observed to decrease the transfer rate by approximately 30%.[36] The smaller value of the nonadiabatic coupling matrix element means that there will be fewer nonadiabatic transitions and smaller nonadiabatic effects for our cluster system. We have computed the fraction of trajectories in the ensemble that undergo zero (adiabatic dynamics), two, four, and six transitions. (Only even numbers of transitions contribute to the diagonal rate in quantum-classical Liouville dynamics.) The majority of the trajectories follow adiabatic dynamics (≈80% of the ensemble), about 10% of the trajectories undergo two nonadiabatic transitions with smaller percentages for higher numbers of transitions. Thus, to a good approximation, the cluster rate coefficients and their dependence on solvent number and temperature can be computed using adiabatic dynamics.

IV. DISCUSSION AND CONCLUSIONS

Proton transfer reactions are strongly influenced by solvation as is evidenced by the fact that the covalent and ionic states of the phenol-amine complex in our study are preferred in the gas and liquid phases, respectively. Our study has shown that the magnitudes of the nanocluster solvation forces can be tuned by changing the temperature or the number of cluster solvent molecules. Thus, cluster simulations can provide useful insight into understanding how the proton transfer process is influenced as the system passes from the gas to the liquid phases.

Our investigations of proton transfer in molecular cluster can be contrasted with those for a similar but simpler symmetric complex model $(A-H\cdots A)^- \rightleftharpoons (A\cdots H-A)^-$ dissolved in larger ($N_s=20-67$) polar molecule clusters.[65] For this model, the free energy profile is symmetric and no vibration of the complex was allowed. For the larger clusters, the complex tended to lie roughly normal to the surface with the strongly ionic end more effectively solvated. Proton transfers were initiated by fluctuations that led to a similar solvation structure for both ends with the complex nearly parallel to the surface. For smaller clusters the complex was almost always found in the interior of the cluster. Although there are similarities in that surface and bulk solvation forces play an important role in the dynamics, the fact that one of the two forms of the phenol-amine complex is covalently bonded while the other is ionically bonded leads to a much stronger correlation between the structure of the cluster and the transfer process.

There are strong similarities between the mechanisms observed in our study and those for proton transfer involving the same phenol-amine model in spherically confined systems that model micelles.[25,26] The ionic form of the complex was found to favor configurations near the surface while the covalent form favored configurations in the interior. An important difference in our cluster systems is that the entire cluster can deform as the transfer process occurs and is coupled with structural changes in the cluster.

It is also interesting to compare our results with the rather different ground-state[66–68] or excited-state[17–22] proton transfer processes that have been studied experimentally in various molecular cluster systems. For example, the inverse proton transfer rate k_{AB}^{-1} was found to be 5 ns for the cluster $PhOH\cdot(NH_3)_4$ but changes dramatically to 55 ps for $PhOH\cdot(NH_3)_5$.[17,18] In these systems the proton transfers to the solvent instead of within the proton-molecule complex. Nevertheless, in our system we observed a similar change in the magnitude of the inverse proton transfer rate. We found that k_{AB}^{-1} increases from 0.1 ns for $N_s=7$ clusters to 30 ps for $N_s=8$ clusters. These results show the strong dependence of the transfer rate on changes in the environmental forces due to changes in the number of cluster molecules.

Nonadiabatic effects on the proton transfer rate were found to be small. This is consistent with observations in earlier studies of this model.[34,36] The contributions of off-diagonal and the excited state matrix elements to the rates are small mainly because the energy gap between the ground and excited states is relatively large for this system. Thus, adiabatic dynamics provides a good approximation to the dynamics, but the situation could change depending on the system details. Nonadiabatic effects are expected to play a larger role for deuteron transfer processes.

The present simulation results have provided insight into the reactive events in nanoclusters. By combining the calculations of equilibrium structure and dynamics, the methodologies described here can be used in more extensive studies including kinetic isotope effects in proton transfer reactions and investigations of hydrated electron dynamics in nanomaterials.

ACKNOWLEDGMENTS

This work was supported in part by a grant from the Natural Sciences and Engineering Council of Canada. We would like to thank Gabriel Hanna for informative discussions and for providing the codes that aided this study.

[1] G. A. Ozin and A. Arsenault, *Nanochemistry: A Chemical Approach to Nanomaterials* (RSC, Cambridge, 2005).
[2] R. P. Bell, *The Proton in Chemistry* (Chapmann and Hall, London, 1973).
[3] S. J. Benkovic and S. Hammes-Schiffer, Science **301**, 1196 (2003).
[4] M. Garcia-Viloca, J. Gao, M. Karplus, and D. G. Truhlar, Science **303**, 186 (2004).
[5] J. K. Hwang and A. Warshel, J. Am. Chem. Soc. **118**, 11745 (1996).
[6] S. Lee and J. T. Hynes, J. Chim. Phys. Phys.-Chim. Biol. **93**, 1783 (1996).

[7] A. Kohen and J. P. Klinman, Acc. Chem. Res. **31**, 397 (1998).
[8] L. I. Krishtalik, Biochim. Biophys. Acta **1458**, 6 (2000).
[9] H. Kim, G. Hanna, and R. Kapral, J. Chem. Phys. **125**, 084509 (2006).
[10] A. W. Castleman and R. G. Keesee, Science **241**, 36 (1988).
[11] R. Pool, Science **248**, 1186 (1990).
[12] A. W. Castleman and K. H. Bowen, J. Phys. Chem. **100**, 12911 (1996).
[13] Q. Zhong and A. W. Castleman, Chem. Rev. (Washington, D.C.) **100**, 4039 (2000).
[14] V. Molinero, D. Laria, and R. Kapral, Phys. Rev. Lett. **84**, 455 (2000).
[15] W. H. Robertson and M. A. Johnson, Annu. Rev. Phys. Chem. **54**, 173 (2003).
[16] T. E. Dermota, Q. Zhong, and A. W. Castleman, Chem. Rev. (Washington, D.C.) **104**, 1861 (2004).
[17] J. Steadman and J. A. Syage, J. Chem. Phys. **92**, 4630 (1990).
[18] J. A. Syage and J. Steadman, J. Chem. Phys. **95**, 2497 (1991).
[19] R. Knochenmuss, G. R. Holtom, and D. Ray, Chem. Phys. Lett. **215**, 188 (1993).
[20] S. K. Kim, J. K. Wang, and A. H. Zewail, Chem. Phys. Lett. **228**, 369 (1994).
[21] J. A. Syage, J. Phys. Chem. **99**, 5772 (1995).
[22] S. K. Kim, J. J. Breen, D. M. Willberg, L. W. Peng, A. Heikal, J. A. Syage, and A. H. Zewail, J. Phys. Chem. **99**, 7421 (1995).
[23] B. Cohen, D. Huppert, K. M. Solntsev, Y. Tsfadia, E. Nachliel, and M. Gutman, J. Am. Chem. Soc. **124**, 7539 (2002).
[24] O. H. Kwon and D. J. Jang, J. Phys. Chem. B **109**, 8049 (2005).
[25] S. M. Li and W. H. Thompson, J. Phys. Chem. B **109**, 4941 (2005).
[26] W. H. Thompson, J. Phys. Chem. B **109**, 18201 (2005).
[27] D. Laria and R. Kapral, J. Chem. Phys. **117**, 7712 (2002).
[28] L. Turi, W. S. Sheu, and P. J. Rossky, Science **309**, 914 (2005).
[29] H. Azzouz and D. Borgis, J. Chem. Phys. **98**, 7361 (1993).
[30] S. Hammes-Schiffer and J. C. Tully, J. Chem. Phys. **101**, 4657 (1994).
[31] D. Antoniou and S. D. Schwartz, J. Chem. Phys. **110**, 465 (1999).
[32] D. Antoniou and S. D. Schwartz, J. Chem. Phys. **110**, 7359 (1999).
[33] R. P. McRae, G. K. Schenter, B. C. Garrett, Z. Svetlicic, and D. G. Truhlar, J. Chem. Phys. **115**, 8460 (2001).
[34] S. Y. Kim and S. Hammes-Schiffer, J. Chem. Phys. **119**, 4389 (2003).
[35] T. Yamamoto and W. H. Miller, J. Chem. Phys. **122**, 044106 (2005).
[36] G. Hanna and R. Kapral, J. Chem. Phys. **122**, 244505 (2005).
[37] I. V. Aleksandrov, Z. Naturforsch. A **36A**, 902 (1981).
[38] V. I. Gerasimenko, Rep. Acad. Sci. Ukr. SSR. **10**, 65 (1981).
[39] V. I. Gerasimenko, Theor. Math. Phys. **50**, 49 (1982).
[40] W. Boucher and J. Traschen, Phys. Rev. D **37**, 3522 (1988).
[41] W. Y. Zhang and R. Balescu, J. Plasma Phys. **40**, 199 (1988).
[42] C. C. Martens and J. Y. Fang, J. Chem. Phys. **106**, 4918 (1997).
[43] R. Kapral and G. Ciccotti, J. Chem. Phys. **110**, 8919 (1999).
[44] M. Santer, U. Manthe, and G. Stock, J. Chem. Phys. **114**, 2001 (2001).
[45] I. Horenko, C. Salzmann, B. Schmidt, and C. Schutte, J. Chem. Phys. **117**, 11075 (2002).
[46] Q. Shi and E. Geva, J. Chem. Phys. **120**, 10647 (2004).
[47] R. A. Marcus and N. Sutin, Biochim. Biophys. Acta **811**, 265 (1985).
[48] A. Warshel, J. Phys. Chem. **86**, 2218 (1982).
[49] D. Laria, G. Ciccotti, M. Ferrario, and R. Kapral, J. Chem. Phys. **97**, 378 (1992).
[50] T. Yamamoto, J. Chem. Phys. **33**, 281 (1960).
[51] H. Kim and R. Kapral, J. Chem. Phys. **122**, 214105 (2005).
[52] H. Kim and R. Kapral, J. Chem. Phys. **123**, 194108 (2005).
[53] A. Sergi and R. Kapral, J. Chem. Phys. **121**, 7565 (2004).
[54] H. Kim and R. Kapral, Chem. Phys. Lett. **423**, 76 (2006).
[55] R. Kapral, Annu. Rev. Phys. Chem. **57**, 129 (2006).
[56] We have neglected the off-diagonal contribution to $W_A^{\alpha' \alpha}$ which we have shown to contribute negligibly to the reaction rate coefficient.
[57] R. Kapral, S. Consta, and L. McWhirter, in *Classical and Quantum Dynamics in Condensed Phase Simulations*, edited by B. J. Berne, G. Ciccotti, and D. F. Coker (World Scientific, Singapore, 1998), pp. 583–616.
[58] R. Kapral and G. Ciccotti, in *In Bridging Time Scales: Molecular Simulations for the Next Decade*, edited by P. Nielaba, M. Mareschal, and G. Ciccotti (Springer-Verlag, Berlin, 2002), pp. 445–472.
[59] M. P. Allen and D. J. Tildesley, *Computer Simulation of Liquids* (Oxford University Press, Oxford, 1987).
[60] D. Frenkel and B. Smit, *Understanding Molecular Simulation: From Algorithms to Applications* (Academic, San Diego, 1996).
[61] E. A. Carter, G. Ciccotti, J. T. Hynes, and R. Kapral, Chem. Phys. Lett. **156**, 472 (1989).
[62] W. K. den Otter and W. J. Briels, J. Chem. Phys. **109**, 4139 (1998).
[63] G. Ciccotti, R. Kapral, and E. Vanden-Eijnden, ChemPhysChem **6**, 1809 (2005).
[64] D. MacKernan, R. Kapral, and G. Ciccotti, J. Phys.: Condens. Matter **14**, 9069 (2002).
[65] S. Consta and R. Kapral, J. Chem. Phys. **104**, 4581 (1996).
[66] M. Meuwly, A. Bach, and S. Leutwyler, J. Am. Chem. Soc. **123**, 11446 (2001).
[67] M. Meuwly and M. Karplus, J. Chem. Phys. **116**, 2572 (2002).
[68] A. Bach, C. Tanner, C. Manca, H. M. Frey, and S. Leutwyler, J. Chem. Phys. **119**, 5933 (2003).